

RESEARCH LETTER

10.1002/2015GL064780

Key Points:

- Bidirectional reflectance of ice/lunar regolith simulant binary mixtures measured in the laboratory
- Strong VIS-NIR signature of ice at high phase angle could be used to detect ice on the surface
- The effect of particle size in common reflectance models is tested

Supporting Information:

- Texts S1 and S2 and Figures S1 and S2

Correspondence to:

Z. Yoldi,
zurine.yoldi@space.unibe.ch

Citation:

Yoldi, Z., A. Pommerol, B. Jost, O. Poch, J. Gouman, and N. Thomas (2015), VIS-NIR reflectance of water ice/regolith analogue mixtures and implications for the detectability of ice mixed within planetary regoliths, *Geophys. Res. Lett.*, 42, 6205–6212, doi:10.1002/2015GL064780.

Received 3 JUN 2015

Accepted 16 JUL 2015

Accepted article online 31 JUL 2015

Published online 12 AUG 2015

VIS-NIR reflectance of water ice/regolith analogue mixtures and implications for the detectability of ice mixed within planetary regoliths

Zuriñe Yoldi¹, Antoine Pommerol¹, Bernhard Jost¹, Olivier Poch^{1,2}, Julien Gouman¹, and Nicolas Thomas¹
¹Physikalisches Institut, Universität Bern, Bern, Switzerland, ²Center for Space and Habitability, Bern, Switzerland

Abstract Permanently shadowed regions at the poles of the Moon and Mercury have been pointed out as candidates for hosting water ice at their surface. We have measured in the laboratory the visible and near infrared spectral range (VIS-NIR) bidirectional reflectance of intimate mixtures of water ice and the JSC-1A lunar simulant for different ice concentrations, particle sizes, and measurement geometries. The nonlinearity between the measured reflectance and the amount of ice in the mixture can be reproduced to some extent by the mixing formulas of standard reflectance models, in particular, those of Hapke and Hiroi, which are tested here. Estimating ice concentrations from reflectance data without knowledge of the mixing coefficients—strongly dependent on the size/shape of the grains—can result in large errors. According to our results, it is possible that considerable amounts of water ice might be intimately mixed in the regolith of the Moon and Mercury without producing noticeable photometric signatures.

1. Introduction

Through the last decade a lot of effort has been made to identify water ice in polar-shadowed areas of Mercury and the Moon, by taking advantage of the synergy between different techniques such as radar imaging, neutron spectrometry, and laser altimetry. Laser altimeters are primarily designed to measure the topography of the studied body but can also retrieve the zero-phase reflectivity of a surface at the wavelength of the instrument (usually 1064 nm) as a by-product [Sun *et al.*, 2006]. Since the addition of ice into a soil or regolith is likely to change its reflectivity, laser altimetry could detect it. This is particularly useful for permanently shadowed regions at the poles of the Moon and Mercury, which are good candidates for hosting ices but where passive remote-sensing methods, such as imaging and reflectance spectroscopy, cannot be used. The Lunar Orbiter Laser Altimeter (LOLA) [Smith *et al.*, 2010] and the Mercury Laser Altimeter (MLA) [Cavanaugh *et al.*, 2007] have characterized the surfaces of the Moon and Mercury, respectively. In the future, the BepiColombo Laser Altimeter [Thomas *et al.*, 2007] will provide further information about the surface of Mercury. Both LOLA and MLA have shown variations in the reflectance of some polar areas of the Moon [Lucey *et al.*, 2014] and Mercury [Neumann *et al.*, 2013] where water ice is thought to exist.

In the case of the Moon, Lucey *et al.* [2014] identified water ice as the most likely candidate for the variable surface reflectance. They also explore the possibility of finding ice mixed within the regolith (i.e., as an intimate mixture), as previously suggested by Feldman *et al.* [2001] and Haruyama *et al.* [2008b].

Direct imaging provides another way of detecting ice. Sensitive cameras can obtain images using indirect illumination from light scattered from opposite crater walls and/or surrounding topography. At Mercury, the MESSENGER's Mercury Dual Imaging System [Hawkins *et al.*, 2007] has imaged the floors of candidate ice-hosting craters, as the Terrain Camera onboard the Selenological and Engineering Explorer [Haruyama *et al.*, 2008a] has done for the Moon. For Mercury, Chabot *et al.* [2014] showed evidences for superficial ice in some craters, whereas Haruyama *et al.* [2008b] conclude that a maximum of 1–2 wt % of water ice might be mixed in the soil of Shackleton Crater in the Moon.

Several authors have studied the reflectance of ice-free binary mixtures. Some of the existing models have been shown to work successfully, so that they can be used for estimating the abundances of the mixture components. In planetary sciences, the Hapke model [Hapke, 1981, 1986, 1993, 2002, 2008] is widely used, both for dry and icy materials and surfaces. Mustard and Pieters [1987, 1989] and Hiroi and Pieters [1994]

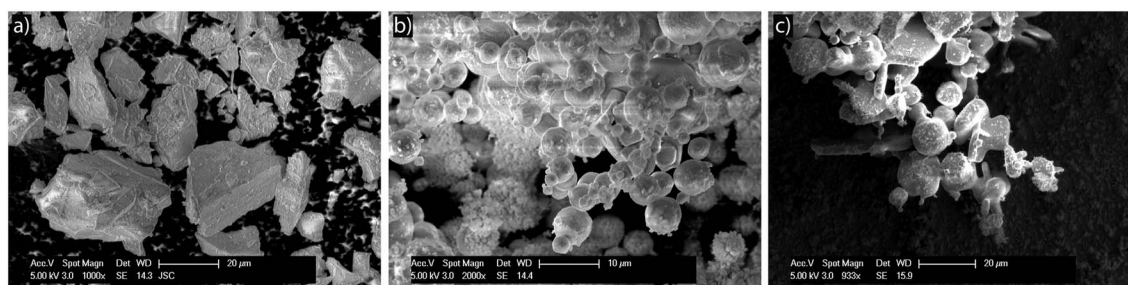


Figure 1. Cryo-SEM images of (a) JSC-1AF, (b) fine-grained ice, and (c) JSC-1AF and fine ice mixture.

proved in the laboratory its accuracy for mixtures of minerals. Another model used here is the model proposed by *Hiroi and Takeda* [1990] and *Hiroi and Pieters* [1992, 1994].

We have produced ice-bearing intimate mixtures in the laboratory and studied their bidirectional reflectance for different geometries. Measurements at zero phase angle are relevant for applications to laser altimetry, whereas measurements at higher phase angle are relevant for the case of indirect illumination of the surface by scattered light. We have tested the two reflectance models mentioned on our samples. As water ice has very different physical properties from the nonvolatile materials previously tested, our aim here is to check if the methods used for dry mixtures can be used for icy mixtures. This is important because recent studies have used these methods to estimate the quantity of ice present at the surfaces of some lunar craters [*Haruyama et al.*, 2008b; *Lucey et al.*, 2014].

In section 2, we describe the preparation of the samples as well as the measurement procedure. Our reflectance results and comparison with models are presented in sections 3 and 4, respectively. Finally, we summarize the main results and detail future perspectives in section 5.

2. Data and Methods

2.1. Components and Mixing Process

All samples studied in this paper consist of mixtures of JSC-1AF lunar regolith simulant and water ice. JSC-1AF is the fine fraction of the lunar mare regolith simulant distributed by the NASA Johnson Space Center, with an average particle size of $24\text{ }\mu\text{m}$ [*Schrader et al.*, 2009]. We have produced two types of water ice with different particle sizes by using two different techniques with the SPIPA (Setup for Preparation of Icy Planetary Analogues) facility. First, we used the setup presented in the supporting information (S1), which produces spherical ice particles with a diameter of $4.5 \pm 2.5\text{ }\mu\text{m}$ by freezing a suspension of very fine droplets of liquid water produced by an ultrasonic inhalator in cold air. Second, we have produced a spray of larger liquid droplets (diameter: $70 \pm 30\text{ }\mu\text{m}$) directed toward a large volume of liquid nitrogen, a technique presented in detail in the supporting information (S1). These two types of water ice particles will be referred to as fine-grained and coarse-grained ice, respectively, in the rest of this manuscript. Ice samples, as well as JSC-1AF and the mixtures, have been characterized by using a cryogenic scanning electron microscope (SEM) (Figure 1).

The procedure for sample preparation was accurately defined and precisely followed for all samples in order to guarantee a good reproducibility and mitigate the influence of preparation on the reflectance of the sample [*Pommerol et al.*, 2013]. Independent of the quantity of sample ultimately needed, we always started by producing the same amount of fresh ice in a given time just before mixing it with the regolith simulant. This was done to limit the possible sintering of the ice particles [*Jost et al.*, 2013]. The ice and JSC-1AF were mixed within an aluminum bottle over a vortex shaker, always for the same time and repeatedly cooled down in liquid nitrogen. In this way, we obtained very homogenous mixtures for both types of ice. Figure 1c shows a cryo-SEM image of the result of the mixing where we can see the JSC-1AF simulant and fine-grained ice intimately mixed at the particle scale. The sample holder was always filled in the same way; first, we filled it with a cooled spoon and then took away the excess with a trowel, without flattening the sample. A last layer of mixture was sieved upon the surface. The openings of the sieve used for this purpose were large enough so that they did not introduce inhomogeneities in the sample. Finally,

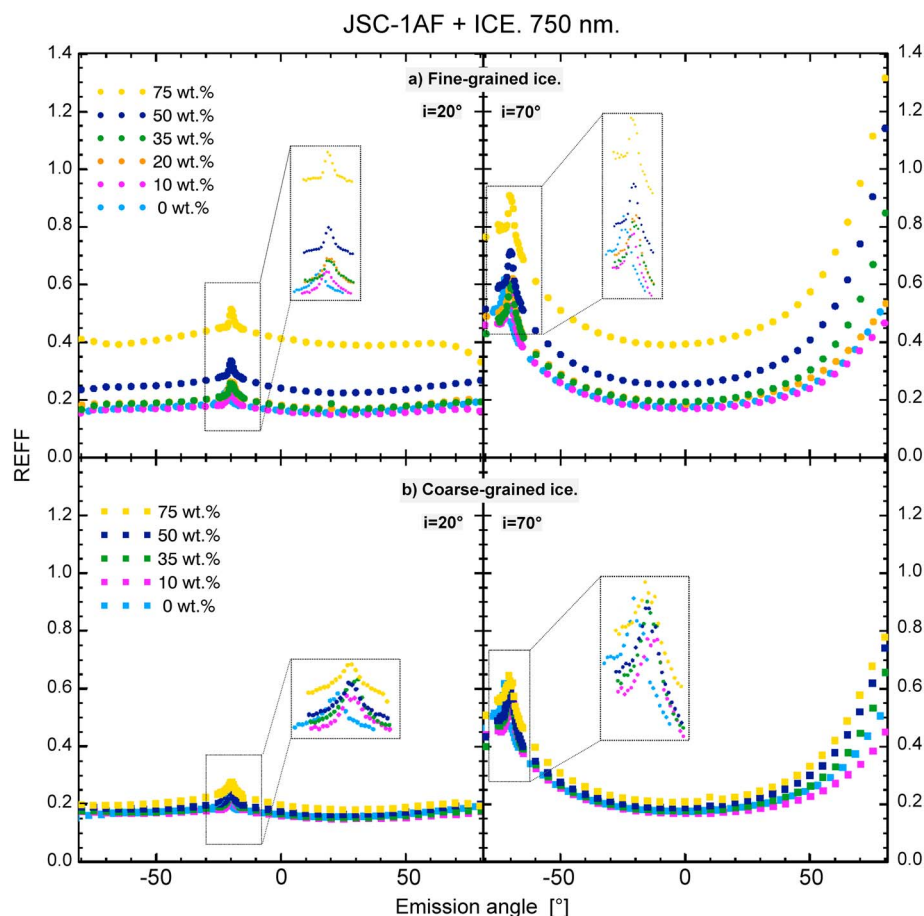


Figure 2. Reflectance phase curves for binary mixtures of JSC-1AF and (a) fine- and (b) coarse-grained ice. Measurements are made at 750 nm and $i = 20^\circ$ and $i = 70^\circ$. Blue symbols show the results for pure JSC1-AF, purple for samples containing a 10 wt % of ice, orange a 20 wt % (only for fine-grained ice), green 35 wt %, dark blue 50 wt %, and yellow 75 wt % of ice. The reflectance peaks correspond to the opposition effect ($g = 0^\circ$), and they have been isolated to show their shape. Please note that this has been done to help the reader to resolve the peak shape and that the absolute scale is not respected.

the sample holder was transported from the preparation freezer to the measurement freezer, a step that lasted not longer than few seconds. This protocol guarantees the reproducibility of the samples and, therefore, of the results.

2.2. Measurement Procedures

All the measurements have been performed with the PHIRE-2 instrument, a gonio-radiometer that permits the characterization of the Bidirectional Reflectance Distribution Function of ice-bearing samples in the visible light spectrometer-near-infrared (VIS-NIR) (400–1100 nm) spectral range. A complete description of the instrument and its performances is given by Pommerol *et al.* [2011]. Recently, the receptor of the instrument has been replaced by a beam splitter head, permitting measurements of the reflectance at very low phase angle.

The PHIRE-2 instrument achieves its peak signal-to-noise ratio (SNR) at 750 nm. Working at this wavelength allows us to perform measurements faster, which is a necessity when working with fine-grained ice samples that evolve quickly by sublimation and sintering. We have seen that for both JSC1-AF and water ice, the reflectance factor (REFF, defined in Hapke [1993]) is comparable at 750 and 1064 nm (see supporting information, Text S2.1). Because of the lower SNR at 1064 nm, acquiring measurements at this wavelength takes 5 times longer than at 750 nm. The less time we spend measuring, the less influence sintering has on the reflectance. For this reason, all measurements in this study have been performed at 750 nm. The average temperature at which measurements have been done was 240 K.

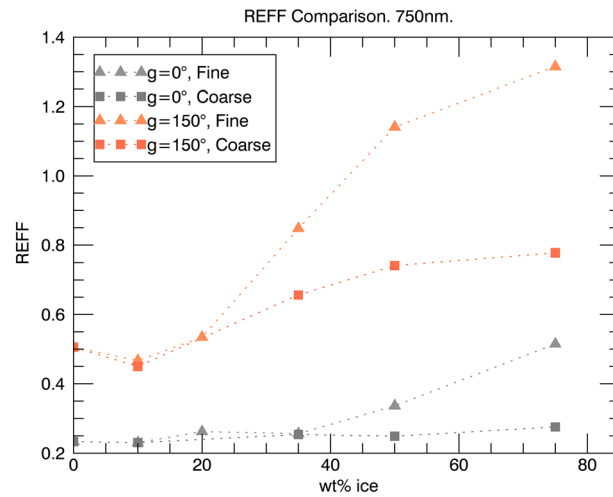


Figure 3. REFF comparison between low and high phase angles, and between fine- and coarse-grained ice for different ice concentrations. Triangles represent the fine ice and squares represent the coarse-grained ice. Greyish tones are used for the zero phase angle whereas orange tones are used for the 150° phase angles. Uncertainties are ~2%.

The data were calibrated in several steps that allow us to compute the stray light, energy losses, etc. A Spectralon reflectance target was used to have an absolute reference for the voltage-reflectance conversion. Further explanation about the calibration process is given in the supporting information (Text S2). The accuracy of the measurements was derived from the data by applying the reciprocity principle, permuting the position of the source and detector [Pommerol *et al.*, 2013]. The relative error observed is ~2%.

We have measured the REFF at low (20°) and high (70°) incidence angles and for emission angles varying between –80° and 80° in the principal plane. Laser altimeters operate by design at low incidence angle, mostly in nadir-viewing geometry. Although the PHIRE-2 instrument permits measurements at normal incidence, measuring at low but nonzero incidence results in more accurate

measurements because of the higher mechanical accuracy of the goniometer. We therefore decided to measure low incidence phase curves at an incidence angle of 20°. Only very minor differences are expected between measurements performed at 0° and 20° incidence angles (Figure S2). Phase curves measured at high incidence angle are interesting to understand the scattering behavior of the regolith analogues at large phase angle, which is relevant for imaging of the floor of polar craters illuminated by light scattered from the local topography. Studying the zero-phase angle geometry allows us to compare our measurements with the ones performed by the laser altimeters and to study the opposition peak shown by the samples at this geometry [Hapke, 1993]. We have used an angular sampling of 5° in emission angle for phase angles larger than 5° but a higher sampling of 0.5° at lower phase angle to better analyze the opposition peak.

3. Results

Phase curves presenting the reflectance as a function of the emission angle are shown in Figure 2, for low (20°) and high (70°) incidence angles. Figure 2a shows the results for fine-grained ice and Figure 2b for

Table 1. Parameters Used for the Reflectance Models

	JSC-1AF	Fine-Grained Ice	Coarse-Grained Ice
HAPKE	$\omega_{JSC-1AF} = 0.77^a$ $\rho_{JSC-1AF} = 2.92 \text{ g/cm}^3^b$ $D_{1_BLUE} = 24 \mu\text{m}$ $D_{1_GOLD} = 1.5 \mu\text{m}$ $D_2/D_{1_ORANGE} = 1$	$\omega_{ICE} = 1.0^a$ $\rho_{ICE} = 0.9168 \text{ g/cm}^3$ $D_{2_BLUE} = 4.5 \mu\text{m}$ $D_{2_GOLD} = 4.5 \mu\text{m}$ $D_2/D_{1_ORANGE} = 1$	$\omega_{ICE} = 1.0^a$ $\rho_{ICE} = 0.9168 \text{ g/cm}^3^c$ $D_{2_BLUE} = 70 \mu\text{m}$ $D_{2_GOLD} = 70 \mu\text{m}$ $D_2/D_{1_ORANGE} = 1$
HIROI	$n_{JSC-1AF} = 1.7^e$ $\alpha_1 = 0.02^g$ $\delta_1 = 5.93 \mu\text{m}$ $\delta_{1_EFF} = 11.86 \mu\text{m}$	$\omega_1 = 0.67^d$ $n_{ICE} = 1.3^f$ $\alpha_2 = 10^{-6g}$ $D_2 = 4.5 \mu\text{m}$ $D_{2_EFF} = 3.015 \mu\text{m}$	$\omega_2 = 0.035^d$ $n_{ICE} = 1.3^f$ $\alpha_2 = 10^{-6g}$ $D_2 = 70 \mu\text{m}$ $D_{2_EFF} = 46.9 \mu\text{m}$

^aFitted by the Hapke Model.

^bAlshibli and Hasan [2009].

^cPounder [1965].

^dOptimized to give the best fit.

^eBrouet [2013].

^fWarren and Brandt [2008].

^gFitted by the Hiroi Model.

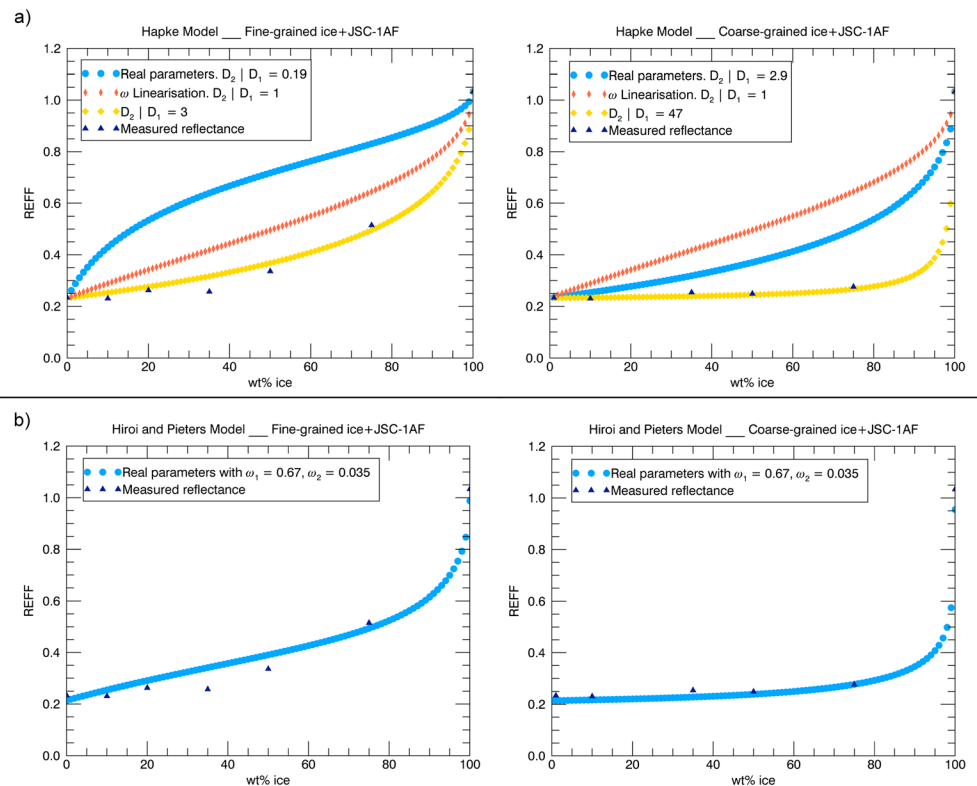


Figure 4. Comparison of the measured data with the (a) Hapke and (b) Hiroi models. The graphs on the left represent the fine ice whereas the right one represents the coarse-grained ice. The parameters used for each case are summarized in Table 1.

coarse-grained ice. In both cases we see that the phase curves measured at low incidence angle are dominated by the opposition effect (occurring at -20° and -70° emission angles, respectively), which produces a relatively strong increase of reflectance (25%) as the phase decreases below 10° . For $i = 70^\circ$, the reflectance increases as well at high phase angle and, for ice-rich samples, reaches a maximum in the forward scattering direction.

In order to study in more detail the relationship between the reflectance and the composition of the sample we extract the reflectance at 0° phase angle for $i = 20^\circ$ and 150° phase angle for $i = 70^\circ$ and plot it as a function of the amount of ice in the binary mixture (Figure 3). Again, for both fine-grained and coarse-grained ice we observe that, when mixed intimately, relatively high amounts of ice within the sample do not significantly affect its reflectance. When looking at the fine-grained ice we see that samples containing up to 35 wt % of ice show almost the same reflectance as ice-free samples. It is only with 50 wt % of ice or more that the reflectance starts to rise and can be differentiated from the ice-free samples. Even higher amounts of ice are required to produce a photometric signature when coarse-grained ice is used. In this case, even a sample containing 75 wt % of ice (88% volume fraction) is not distinguishable from an ice-free sample. The reflectance measured at high phase angle, however, shows a much stronger dependence on the amount of ice in the sample.

4. Discussion

Our results demonstrate, in a few particular cases, how difficult it is to detect water ice intimately mixed within a lunar-type regolith from its VIS-NIR photometric signature. For example, looking at a surface at 0° phase and low incidence angle, one would not be able to distinguish between a dry soil and a soil containing up to 75 wt % of $100\mu\text{m}$ sized water ice particles. It is important to highlight this, since in the scientific literature we often find the idea that, with only a small wt % of water ice mixed within the soil, the reflectance rises, and thus, a low albedo implies a relatively small quantity of ice [Haruyama et al., 2008b;

Zuber *et al.*, 2012]. The results presented here set the detection threshold for particulate water ice mixed intimately into the regolith much higher. The reflectance results for $i=70^\circ$ show that high phase angles provide the best chance of detecting water ice because of the strong forward scattering peak in ice-rich samples. We suggest that, when the sunlight that is scattered from the illuminated crater walls reaches the ice in the shadow with large incidence angles, an orbital camera could detect, with a large exposure time, the increase of reflectance produced by the forward scattering. This intensity increases greatly with the ice content and would therefore be a strong indicator of the presence of exposed ice.

In order to expand our experimental findings from a few particular cases to more general trends, we use our data to test and calibrate existing reflectance models. This is crucial to establish whether we can determine precisely the quantity of water ice found in the lunar and/or Hermean craters. We have tested the widely used reflectance model from Hapke [1981] and that from Hiroi and Takeda [1990]. These models use different approaches to compute the reflectance of a binary intimate mixture from the properties of the components. As previously stated by Clark [1981], we have seen that the size of the ice particles strongly affects the reflectance, so we focus on how each model deals with parameters such as the size and shape of the end-members. The parameters that we have used for each model are shown in Table 1. All the reflectance values in Figure 4 are the reflectance results for $i=20^\circ$ and 0° phase angles.

4.1. The Hapke [1981] Model

In Hapke's model of the single scattering albedo (ω) of a multicomponent medium is given by Hapke [1981, equation (17)], which, in the case of a binary mixture of spherical particles—or particles with approximately the same shape—can be arranged as follows [Hapke, 1993]:

$$\omega = \frac{\zeta \omega_1 + \omega_2}{1 + \zeta} \quad \text{with} \quad \zeta = \frac{M_1 \rho_2 D_2}{M_2 \rho_1 D_1}, \quad (1)$$

where ω_i is the single scattering albedo, M_i is the bulk density, ρ_i is the solid density, and D_i the mean diameter of the particles of each component. In order to study the influence of the size of the particles, the other parameters have been fixed with the values shown in Table 1. Different size ratios have been tested; Figure 4a shows the results of the Hapke model predictions for those ratios and compares them with our results for $i=20^\circ$ and 0° phase angles. For both fine- and coarse-grained ice, the blue line represents the actual values of our end-members, while the gold one exaggerates the size difference between the JSC-1AF and the ice by making the basalt smaller. Finally, the orange line shows the result of linearizing the single scattering albedo, i.e., setting $D_2/D_1 = 1$.

Real mean diameters do not give the best modeled estimates of the reflectance; the data are better fitted when we run the model with smaller JSC-1AF particles. This is certainly an effect of the difference of shape between irregular basalt particles and spherical ice particles (Figure 1a), so that the effective scatterer size is much smaller than the average grain size in the case of the regolith simulant. Hapke [1993] already stated that when dealing with irregular particles, the equivalent radius should be determined by the cross section of the particle, which is consistent with the results shown here. Consequently, the model's best estimate is found for a particle size of $1.5 \mu\text{m}$ instead of $24 \mu\text{m}$. On the surface of the Moon or Mercury, we can expect such a contrast of shape between the ice and basalt particles, since it is a direct effect of the contrast of physical properties between a refractory and a volatile element, the first one having condensed billions of years ago and subjected to surface alteration for a long time, while the second one is subject to cycles of sublimation and condensation.

4.2. The Hiroi Model

Hiroi and Takeda [1990] proposed a model where they treat the reflectance of a particulate surface as a series of grain interactions. One of the strengths of this model is that it introduces a shape factor. Depending on the shape of the particle (spherical, cubical, or disk shape), a different effective grain size can be computed [Hiroi and Pieters, 1992, Figure 13]. As we see in Figure 1, the ice that we use has a spherical shape, while the particles of JSC-1AF can be approximated as disks. This model has two free parameters (ω_1 and ω_2) that are adjusted to find the best fit. By using the effective grain size that corresponds to each type of particle and the parameters summarized in Table 1, we obtain the curves shown in Figure 4b. The presence of two free parameters implies that a good fit can be obtained even for nonrepresentative sizes of grains. Still, we have seen that once ω_1 and ω_2 have been fixed for a set of data (i.e., fine ice), the same values can be

used for the same material but different sizes (i.e., coarse ice), which is useful for extrapolating the laboratory measurements.

5. Conclusions

Experimental results show that ice mixed intimately within a regolith is more difficult to detect when it is present as bigger particles and when it is observed at low incidence and phase angles. At low incidence angles and zero-phase angle it would not be possible to distinguish a soil containing up to 75 wt % of ice from an ice-free soil. Observing the surface at higher phase angles results in a higher probability of detection; when possible, orbital cameras with very high signal-to-noise ratios would be a better choice to detect particulate water ice than laser altimeters.

Quantitative estimates of the amount of ice in the regolith of lunar and/or Hermean polar craters derived from reflectance models should be taken with caution. Models work well in a relative way, as they are able to reproduce the shape of the relationship between the reflectance and the composition. These relationships are strongly influenced by mixing parameters, which are dependent on the sizes and shapes of the particles. The omission of the size factor in Hapke's model in order to linearize the single scattering albedos leads to large errors. Regarding the shape, we have seen that treating both irregular (basalt) and smooth (ice) shapes in the same way leads to wrong estimations, since the effective scatterer size depends on the geometry of the particles. That is why, when taking into account the irregularities of the particles in Hapke's model and assuming a smaller mean optical path length, the model can fit the data. Also, the model of Hiroi which takes into account the effective scattering size of the particles gives, once the model is calibrated, a good fit.

Regarding the Moon, an accurate estimation of the water ice found in the polar craters will be possible when we know more about the properties of the lunar soil and ice in the regolith. In any case, this study is a step forward to the objective of water ice estimation, since we now know that there might be much more water ice in the lunar polar regions than current estimations suggest [Lucey *et al.*, 2014; Haruyama *et al.*, 2008b; Zuber *et al.*, 2012].

Acknowledgments

This work was financed by the Swiss National Science Foundation under the NCCR PlanetS and grant 200020_152560. There are no data sharing issues as the figures provide the measurements on which the conclusions are based. The numerical data will be made available upon request by mail to the corresponding author.

The Editor thanks Takahiro Hiroi and an anonymous reviewer for their assistance in evaluating this paper.

References

- Alshibli, K., and A. Hasan (2009), Strength properties of JSC-1A lunar regolith simulant, *J. Geotech. Geoenviron. Eng.*, 135(5), 673–679.
- Brouet, Y. (2013), Contribution à la détermination de la permittivité des noyaux cométaires et des astéroïdes, PhD thesis, Univ. Pierre et Marie Curie, France.
- Cavanaugh, J. F., et al. (2007), The Mercury laser altimeter instrument for the MESSENGER Mission, in *The Messenger Mission to Mercury*, edited by D. L. Domingue and C. T. Russell, pp. 451–479, Springer, New York, doi:10.1007/978-0-387-77214-1_1.
- Chabot, N. L., et al. (2014), Images of surface volatiles in Mercury's polar craters acquired by the MESSENGER spacecraft, *Geology*, 42, 1051–1054, doi:10.1130/G35916.1.
- Clark, R. N. (1981), Water frost and ice: The near-infrared spectral reflectance 0.65–2.5 μm , *J. Geophys. Res.*, 86(B4), 3087–3096, doi:10.1029/JB086iB04p03087.
- Feldman, W. C., et al. (2001), Evidence for water ice near the lunar poles, *J. Geophys. Res.*, 106(E10), 23, 231–23,251, doi:10.1029/2000JE001444.
- Hapke, B. (1981), Bidirectional reflectance spectroscopy: 1 Theory, *J. Geophys. Res.*, 86(B4), 3039–3054, doi:10.1029/JB086iB04p03039.
- Hapke, B. (1986), Bidirectional reflectance spectroscopy. IV-The extinction coefficient and the opposition effect, *Icarus*, 67(2), 264–280, doi:10.1016/0019-1035(86)90108-9.
- Hapke, B. (1993), *Theory of Reflectance and Emittance Spectroscopy: Topics in Remote Sensing*, Cambridge Univ. Press, Cambridge, U. K.
- Hapke, B. (2002), Bidirectional reflectance spectroscopy: 5 The coherent backscatter opposition effect and anisotropic scattering, *Icarus*, 157, 523–534.
- Hapke, B. (2008), Bidirectional reflectance spectroscopy: 6. Effects of porosity, *Icarus*, 195, 918–926.
- Haruyama, J., T. Matsunaga, M. Ohtake, T. Morota, C. Honda, Y. Yokota, M. Torii, Y. Ogawa, and the LISM Working Group (2008a), Global lunar-surface mapping experiment using the Lunar Imager/Spectrometer on SELENE, *Earth Planets Space*, 60, 243–255.
- Haruyama, J., et al. (2008b), Lack of exposed ice inside lunar south pole Shackleton crater, *Science*, 322(5903), 938–939, doi:10.1126/science.1164020.
- Hawkins, S. E., III et al. (2007), The Mercury dual imaging system on the MESSENGER spacecraft, *Space Sci. Rev.*, 131(1–4), 247–338, doi:10.1007/s11214-007-9266-3.
- Hiroi, T., and C. M. Pieters (1992), Effects of grain size and shape in modeling reflectance spectra of mineral mixtures, *Proc. Lunar Planet. Sci.*, 22, 313–325.
- Hiroi, T., and C. M. Pieters (1994), Estimation of grain sizes and mixing ratios of fine powder mixtures of common geologic minerals, *J. Geophys. Res.*, 99(E5), 10,867–10,879, doi:10.1029/94JE00841.
- Hiroi, T., and H. Takeda (1990), A method to determine silicate abundances from reflectance spectra with applications to asteroid 29 amphitrite associating it with primitive achondrite meteorites, *Icarus*, 88, 205–227.
- Jost, B., B. Gundlach, A. Pommerol, J. Oesert, S. N. Gorb, J. Blum, and N. Thomas (2013), Micrometer-sized ice particles for planetary-science experiments: II. Bidirectional reflectance, *Icarus*, 225(1), 352–366, doi:10.1016/j.icarus.2013.04.007.
- Lucey, P. G., et al. (2014), The global albedo of the Moon at 1064 nm from LOLA, *J. Geophys. Res. Planets*, 119, 1665–1679, doi:10.1002/2013JE004592.

- Mustard, J. F., and C. M. Pieters (1987), Quantitative abundance estimates from bidirectional reflectance measurements, *J. Geophys. Res.*, 92(B4), e617–e626, doi:10.1029/JB092iB04p0E617.
- Mustard, J. F., and C. M. Pieters (1989), Photometric phase functions of common geologic minerals and applications to quantitative analysis of mineral mixture reflectance spectra, *J. Geophys. Res.*, 94(B10), 13,619–13,634, doi:10.1029/JB094iB10p13619.
- Neumann, G. A., et al. (2013), Bright and dark polar deposits on Mercury: Evidence for surface volatiles, *Science*, 339, 296–300, doi:10.1126/science.1229764.
- Pommerol, A., N. Thomas, M. Affolter, G. Portyankina, B. Jost, K. Seiferlin, and K.-M. Aye (2011), Photometry and bulk physical properties of Solar System surfaces icy analogs: The Planetary Ice Laboratory at University of Bern, *Planet. Space Sci.*, 59, 1601–1612, doi:10.1016/j.pss.2011.07.009.
- Pommerol, A., N. Thomas, B. Jost, P. Beck, C. Okubo, and A. S. McEwen (2013), Photometric properties of Mars soils analogs, *J. Geophys. Res. Planets*, 118, 2045–2072, doi:10.1002/jgre.20158.
- Pounder, E. R. (1965), *The Physics of Ice*, Elsevier, Oxford, U. K.
- Schrader, C. M., D. L. Rickman, C. A. McEwen, J. C. Fikes, D. B. Stoeser, S. J. Wentworth, and D. S. McKay (2009), Lunar regolith characterization for simulant design and evaluation using figure of merit algorithms, in Proc., 47th AIAA Aerospace Sciences Meeting, ISO 690.
- Smith, D. E., et al. (2010), The Lunar orbiter laser altimeter investigation on the lunar reconnaissance orbiter mission, *Space Sci. Rev.*, 150, 209–241, doi:10.1007/s11214-009-9512-y.
- Sun, X., G. A. Neumann, J. B. Abshire, and M. T. Zuber (2006), Mars 1064 nm spectral radiance measurements determined from the receiver noise response of the Mars Orbiter Laser Altimeter, *Appl. Opt.*, 45, 3960–3971.
- Thomas, N., et al. (2007), The BepiColombo Laser Altimeter (BELA): Concept and baseline design, *Planet. Space Sci.*, 55, 1398–1413, doi:10.1016/j.pss.2007.03.003.
- Warren, S. G., and R. E. Brandt (2008), Optical constants of ice from the ultraviolet to the microwave: A revised compilation, *J. Geophys. Res.*, 113, D14220, doi:10.1029/2007JD009744.
- Zuber, M. T., et al. (2012), Constraints on the volatile distribution within Shackleton crater at the lunar south pole, *Nature*, 486, 378–382, doi:10.1038/nature11216.